

Thrust Control for Multirotor Aerial Vehicles

Moses Bangura, *Student Member, IEEE*, and Robert Mahony, *Fellow, IEEE*

Abstract—This paper presents a novel control algorithm to regulate the aerodynamic thrust produced by fixed-pitch rotors commonly used on small-scale electrically powered multirotor aerial vehicles. The proposed controller significantly improves the disturbance rejection and gust tolerance of rotor thrust control compared to state-of-the-art RPM (revolutions per minute) rotor control schemes. The thrust modeling approach taken is based on a model of aerodynamic power generated by a fixed-pitch rotor and computed in real time on the embedded *electronic speed controllers* using measurements of electrical power and rotor angular velocity. Static and dynamic flight tests were carried out in downdrafts and updrafts of varying strengths to quantify the resulting improvement in maintaining a desired thrust setpoint. The performance of the proposed approach in flight conditions is demonstrated by a path tracking experiment, where a quadrotor was flown through an artificial wind gust and the trajectory tracking error was measured. The proposed approach for thrust control demonstrably reduced the tracking error compared to classical RPM rotor control.

Index Terms—Aerodynamics, brushless direct current motor (BLDC) control, thrust control.

I. INTRODUCTION

THE hierarchical nature of the typical control structure used to control multirotor aerial vehicles has been widely explored [10], [15], [21]. The lowest level of such a hierarchical control structure is the motor–rotor thrust control. The current state-of-the-art model for motor–rotor control is based on the regulation of the rotor angular velocity or RPM (*revolutions per minute*) [26], [27]. In order to regulate thrust, a static aerodynamic model relating rotor speed to thrust for a rotor in static free air is typically used [21]. Static thrust models have proven effective in a wide range of applications, however, they display significant errors in the presence of gusts or when the rotor is moving. The strongest effects are due to vertical motion of the rotor or updrafts and downdrafts, although lateral motion or sideways gusts also cause small variations in rotor thrust. Using CFDs tools, Luo *et al.* [19] showed that for lateral flights with

velocities up to 10 m/s, the maximum power saved associated with the additional translational lift is only 6%. Consequently, a constant power flight will result in less than 6% gain in translational lift. The question of providing effective control for multirotors in the presence of wind gusts, or during fast and aggressive manoeuvres has been raised by a number of recent papers [9], [17], [28], [30]. One approach that has proven to be highly successful for repetitive high-performance aggressive manoeuvres is to use time-varying parameter adaptation and iterative learning [20], [23]. The resulting controller provides a learnt feedforward compensation for the highly nonlinear aerodynamic conditions encountered by each rotor during a given known manoeuvre for which training has been undertaken. In the absence of learning, then it is necessary to either estimate or measure the actual thrust generated by the rotor. Possible approaches include using strain gauges, or directly measuring the airspeed using pitot tubes [3], [31] or estimation of the aerodynamic state using inertial measurement units (IMUs) [2], [24]. Direct force measurement using strain gauges suffer from high frequency and high noise-to-signal ratio [29]. Direct airspeed measurements suffer from accuracy and slow response of pitot tubes. Arain and Kendoul [3] used a single pitot tube to measure the forward velocity of the vehicle, while Yeo *et al.* [31] used four pitot tubes mounted underneath each rotor to measure the axial velocities through the rotors. From results in [3], low airspeed wind estimation for quadrotors is a challenge and the airspeed measurements are unreliable for velocities under 1 m/s. Arain and Kendoul [3] also obtained errors of up to 2 m/s for ground truth forward velocity of 6 m/s. Yeo *et al.* [31] used their wind estimates in designing safe trajectories, though errors were observed of 0.4 m/s for a velocity measurement of 1.5 m/s. More importantly, typical pitot tubes display response times of 100 ms which makes them unsuitable for high-performance control.

Shen *et al.* [28] used a Kalman filter to estimate thrust force in the presence of external disturbances arising from their indoor flight experiments. The 50 Hz limitation in the communication between the flight control board and *electronic speed controllers* (ESC) typical in quadrotor systems limit the performance of such an approach. Another approach that has been proposed is to use analytic implicit models developed from computational fluid dynamics (CFD) [16], [19] to estimate thrust. These methods also consider the effect of wake interference during translational motion of air. The computational load of such an approach is infeasible for small-scale aerial robotic systems.

For marine thrusters, with the assumption of only axial flow, accurate thrust computation/estimation and control is a well-studied problem [6], [14], [25]. In [14], a model that uses the electromechanical dynamics of the motor along with

Manuscript received May 27, 2016; accepted October 26, 2016. Date of publication January 16, 2017; date of current version April 3, 2017. This paper was recommended for publication by Associate Editor R. Eustice and Editor T. Murphey upon evaluation of the reviewers' comments. This work was supported by the Australian Research Council through Discovery Grant DP120100316 "Integrated High-Performance Control of Aerial Robots in Dynamic Environments."

M. Bangura is with the College of Engineering and Computer Science, Australian National University, Canberra, ACT 0200, Australia (e-mail: Moses.Bangura@anu.edu.au).

R. Mahony is with the ARC Centre for Vision Robotics, College of Engineering and Computer Science, Australian National University, Canberra, ACT 0200, Australia (e-mail: Robert.Mahony@anu.edu.au).

Color versions of one or more of the figures in this paper are available online at <http://ieeexplore.ieee.org>.

Digital Object Identifier 10.1109/TRO.2016.2633562

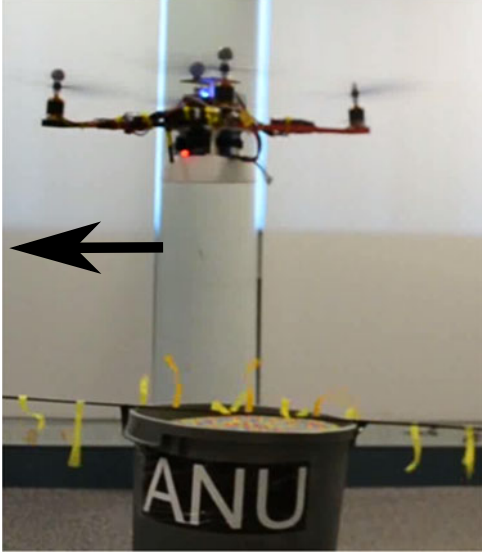


Fig. 1. Quadrotor aerial vehicle used for the experimental results obtained. It is shown flying across a “nearly” laminar flow generator with the new thrust controller. Despite the competing wake of the vehicle and the laminar flow shown by the streamers, its path is undisturbed.

propeller hydrodynamics and thin-foil theory to produce a two-state propulsion model was proposed. Bachmayer *et al.* [6] further developed this model to account for positive and negative flow velocities and proposed a method for generating lift and drag curves to achieve more accurate control. Sørensen *et al.* [25] proposed a controller that does friction compensation and torque limiting through a minimization algorithm that is unfortunately computationally infeasible in real time on existing embedded hardware.

In this paper, we present a scheme for computing and regulating aerodynamic thrust and estimation of the aerodynamic conditions around individual rotors for multirotor aerial vehicles, specifically fixed-pitch electrically powered quadrotors. Fig. 1 shows the experimental platform at the point of flying over a crude flow laminator, a device that generates a laminar flow over an area, in this case, a plastic tube (a rubbish bin with the bottom removed) with an internal fan that forces air through an array of narrow tubes (glued drinking straws) at the upper exit. The paper builds upon the power control approach first presented in [7] and adds to this a more correct blade element momentum model that allows for accurate computation of thrust and airflow rather than just regulation of aerodynamic power. The proposed algorithm is designed to be implemented at high bandwidth directly on the ESC of the vehicle and consequently has low computational complexity and relies primarily on local measurements of DC current, bus voltage, and rotor RPM made available on the ESC. The aerodynamic power dissipated by the rotor is related to the mechanical power supplied to the rotor shaft and in turn to the electrical power supplied to the motor providing a measurement that can be directly controlled. The combination of power and RPM along with a suitable aerodynamic model provides sufficient constraints to estimate the coupled vertical inflow ratio, thrust, and other aerodynamic variables in the rotor flow. Once thrust is computed, a simple and highly robust *proportional integral* (PI) [4] controller is sufficient to

regulate the desired thrust, although an inner high-gain current control loop and feedforward compensation are critical to obtain the required system response. The effectiveness of the proposed approach and controller are validated against a classical RPM controller in static and dynamic flight conditions. The results demonstrate a significant improvement in thrust robustness to downdrafts or updrafts. Furthermore, the performance of a path tracking controller is significantly improved with the proposed control architecture as compared to classical RPM control when subject to gust disturbances.

The remainder of the paper is organized as follows: the aerodynamics of rotors and the proposed power-based implicit thrust computation scheme are presented in Section II. Section III details the control algorithms that regulate a thrust setpoint for a motor-rotor system. In Section IV, we describe laboratory calibration procedures necessary to identify the aerodynamic coefficients of the rotor and electrical parameters of the motor. Section V presents experimental results that demonstrate the performance of the proposed scheme with reference to the standard RPM method.

II. POWER-BASED THRUST MODEL

In this section, we present models for the aerodynamic forces, torque, and power associated with a fixed-pitch rotor using momentum and blade element theories. With these models, we propose an implicit thrust computation scheme for a rotor in relative axial wind motion. The model development uses macroscopic force and torque/power representation initially and then transforms into scalar aerodynamic coefficients that are better suited for use as variables for implementation on an ESC.

A. Problem Formulation

The rotor hub/shaft and rotor blades of a rotor can be represented in three separate frames of reference [11]: the vehicle *body-fixed frame* $\{B\}$, the rotor reference frame $\{C\}$ that rotates with the rotor but does not tilt with blade flapping, and the *tip-path-plane* (TPP) or $\{D\}$. The TPP rotates with the rotor and is also aligned with the tilt of the rotor due to blade flapping and, to first order, the rotor is stationary in this frame. Throughout the paper, $\vec{e}_1, \vec{e}_2, \vec{e}_3$ are used to denote unit vectors in the x, y, z directions, respectively.

Consider the control volume shown in Fig. 2 associated with a slightly tilted actuator disc, a result of the rotor experiencing both translational and axial air motion with velocity $\vec{V} \in \mathbb{R}^3$. This is the relative velocity between the vehicle’s *body-fixed frame* $\{B\}$ and inertial frame $\{A\}$ expressed in $\{B\}$ as shown in Fig. 3. The stream velocity is equal in magnitude but opposite in direction to the vehicle velocity \vec{V} when there is no wind but is the sum when the wind velocity $\vec{W} \in \mathbb{R}^3$ expressed in $\{B\}$ is present, i.e., $\vec{v}^s = -\vec{V} + \vec{W} \in \mathbb{R}^3$. The spinning rotor induces additional air velocity $\vec{v}^i \in \mathbb{R}^3$ through the rotor so that the total air velocity through the rotor \vec{v}^a is $\vec{v}^a = \vec{v}^i + \vec{v}^s$. We denote the velocity of the wake far downstream by \vec{v}^∞ . All these velocities are expressed in $\{B\}$.

Remark 1: The induced velocity on a rotor is a nonuniform distribution and its effect can be modeled by Mangler and Squire method [11], [12], [18]. However, an average value of \vec{v}^i can

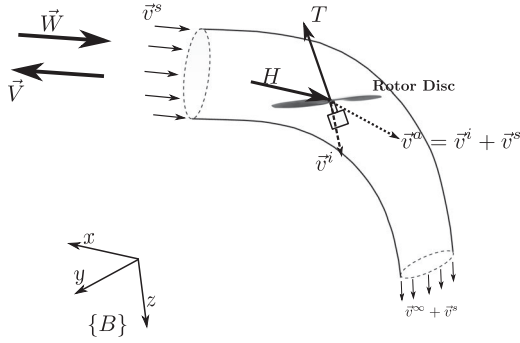


Fig. 2. Rotor control volume along with the streamtube, generated forces, and the different air velocities. The vehicle velocity \vec{V} and wind speed \vec{W} have an apparent stream velocity into the rotor of $\vec{v}^s = -\vec{V} + \vec{W}$. The actual air velocity at the rotor \vec{v}^a is the sum of the induced velocity \vec{v}^i plus the apparent stream velocity \vec{v}^s . The scalar thrust T and scalar drag H are shown in the two-dimensional plane associated with the longitudinal flight dynamics.

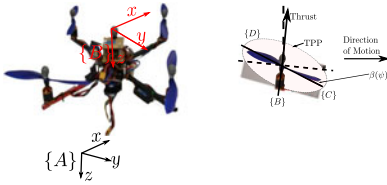


Fig. 3. Different frames of reference of a quadrotor and its rotors. The inertial frame fixed on the earth $\{A\}$ and *body-fixed frame* attached to the vehicle $\{B\}$ along with rotor reference frame $\{C\}$ and tip-path-plane $\{D\}$.

be used in the modeling process in a similar manner to the performance analysis for helicopters [12], [18]. In [11], the authors showed this approximation has no effect on thrust.

If $\vec{F} \in \mathbb{R}^3$ is the total force generated at the rotor mast expressed in the vehicle *body-fixed frame* $\{B\}$, then

$$\vec{F} = -T\vec{e}_3 + \vec{F}_{\text{hor}} \in \{B\}$$

where $T \in \mathbb{R}$ is the axial thrust and $\vec{F}_{\text{hor}} \in \mathbb{R}^3$ is the remaining horizontal vector force. The thrust T generated by the rotor is associated with the component of force \vec{F} in the $-\vec{e}_3$ direction, that is, $T = -\vec{e}_3^\top \vec{F}$. This convention ensures that in normal flight, the thrust T is positive. Note that in most helicopter texts, for example, [12], the thrust is modeled as orthogonal to the *TPP*. However, we find that modeling the thrust in the *body-fixed frame* $-\vec{e}_3$ direction and introducing a horizontal thrust component \vec{F}_{hor} due to the tilting of the thrust vector is a more effective modeling framework for small-scale fixed-pitch rotor systems used in robotic applications. Fig. 2 shows the rotor tilting backward with respect to the rotor shaft as a result of blade flapping. The net effect of rotor flapping is to tilt the lift force generated by the rotor disc and contribute to the horizontal force \vec{F}_{hor} . The horizontal force also comprises other aerodynamic effects such as induced and translational drag [11], [21] that in many cases are even more important than blade flapping for small fixed-pitch rotors used on quadrotor vehicles. Critically, these additional drag forces can be lumped into the same mathematical model used to model flapping [21] (cf. (1)) as long as all forces and velocities are written in the *body-fixed frame* $\{B\}$.

As the air passes through the rotor disc, it is accelerated creating an induced velocity component $\vec{v}^i \in \mathbb{R}^3$. The induced velocity \vec{v}^i of the rotor on the air decomposes into a vertical component $v_z^i = \vec{e}_3^\top \vec{v}^i \in \mathbb{R}$ and a horizontal component $(v_x^i, v_y^i, 0)^\top$ that lies parallel to the horizontal planar velocity $(V_x, V_y, 0)^\top$ of the rotor in $\{B\}$. The accepted model for the horizontal force \vec{F}_{hor} in typical flight conditions is given by [1], [9], [12], [21], [22], [26], [28]

$$\vec{F}_{\text{hor}} \propto -k_{\text{hor}}(V_x, V_y, 0)^\top \quad (1)$$

where k_{hor} is a positive constant at constant T . Since all the aerodynamic variables in the problem lie in the two-dimensional (2-D) (longitudinal flight dynamics) plane defined by the apparent stream velocity \vec{v}^s and rotor hub axes \vec{e}_3 , it is possible to undertake the aerodynamic analysis using these two degrees of freedom (DF) rather than maintaining the full 3-D-velocity and force information. We write $V_h = |V_x, V_y, 0|$ as the scalar magnitude of the *body-fixed frame* horizontal velocity of the rotor and define a *body-fixed frame* direction

$$\vec{e}_{\text{hor}} = \begin{cases} \frac{1}{V_h}(V_x, V_y, 0)^\top & \text{for } V_h \neq 0, \\ (0, 0, 0)^\top & \text{for } V_h = 0 \end{cases}$$

where the zero vector is used to ensure \vec{e}_{hor} is always well defined. Based on this construction, we define scalar values of horizontal induced velocity and the horizontal force

$$v_h^i = \vec{e}_{\text{hor}}^\top \vec{v}^i \in \mathbb{R}, \quad H = -\vec{e}_{\text{hor}}^\top \vec{F} \in \mathbb{R}.$$

Due to the nature of the aerodynamic drag terms, the horizontal force \vec{F}_{hor} always opposes the motion of the vehicle, that is

$$\vec{e}_{\text{hor}}^\top \vec{F} = \vec{e}_{\text{hor}}^\top \vec{F}_{\text{hor}} \leq 0$$

implying $H \geq 0$. Moreover, when $v_h^s = 0$, then $v_x^i = v_y^i = 0$ and the horizontal force $\vec{F}_{\text{hor}} = 0$, yielding $H = 0$ as expected. In the case where $v_h^s - \vec{W}_h \neq 0$, the induced horizontal scalar velocity v_h^i is nonnegative since the rotor tilt opposes the horizontal motion of the rotor hub and consequently the induced component of the velocity will be pushing air against the direction of motion of the rotor. Note that due to the motion of the rotor, the *actual* horizontal component of air through the rotor will be negative as expected (see Fig. 2).

The aerodynamic rotor power P_a is defined to be the power supplied to the air streamtube by the rotor and is a key variable in the following development. It comprises a component due to the induced air velocity and a component due to the stream velocity, that is

$$P_a = \kappa \langle \vec{F}, \vec{v}^i \rangle + \langle \vec{F}, \vec{v}^s \rangle \quad (2)$$

where the scalar $\kappa \geq 1$ is the *induced power factor* [12, pg. 92] [18, pg. 105]. The constant κ is an adjustment factor that models the additional power dissipated due to wake rotation, tip loss effects, and nonuniform inflow that are not modeled by classical momentum theory. It is constant in hover conditions but varies for changing inflow conditions and will be separately modeled in Section II-D. Note that aerodynamic losses only apply to the induced aerodynamic power and not to the power associated

with the physical motion of the rotor. The aerodynamic rotor power is only a part of the total aerodynamic mechanical power P_{am} that dissipates into two aerodynamic terms

$$P_{\text{am}} = P_p + P_a \quad (3)$$

where P_p [12] is the blade profile power associated with aerodynamic drag on the rotor blade and P_a is the aerodynamic rotor power discussed above. A model for profile power will be developed in Section II-C. In summary, the profile power P_p is dissipated energy lost in pulling the rotor through the air, while the aerodynamic power P_a is associated with accelerating the air through the rotor and contributes to thrust generation and associated mechanical power supplied to the rigid airframe.

Remark 2: The induced power factor κ is closely related to, but not the same as, the (inverse of the) well-known *figure of merit* $\eta \in [0, 1]$ [18] used in hover analysis of full-scale helicopters. In the case where horizontal and vertical motion are negligible, then H , V_h , and V_z are small and the dominant term in the aerodynamic power is $\kappa T v_z^i$. The term $T v_z^i$ is the aerodynamic power in the linear part of the wake and is the primary term associated with the momentum theory thrust analysis. Thus, one has $T v_z^i = \frac{1}{\kappa} P_a$. However, this expression does not include losses due to the profile power P_p of the blades. The *figure of merit* η models the aerodynamic mechanical power P_{am} applied to the rotor shaft in ratio to the actual aerodynamic power in the linear stream flow

$$\eta = \frac{T |\vec{v}^a|}{P_{\text{am}}}.$$

That is, η models the losses modeled by $\frac{1}{\kappa}$ as well as the profile drag of the rotor blades [9]. The figure of merit does not provide sufficient discrimination for the analysis we undertake and is not used in this paper.

Define the advance ratio μ and vertical inflow ratio λ as dimensionless scalar variables associated with rotor operation

$$\lambda = \frac{v_z^i + v_z^s}{\varpi R} = \frac{v_z^i}{\varpi R} + \frac{v_z^s}{\varpi R} = \lambda^i + \lambda^s, \quad (4a)$$

$$\mu = \frac{v_h^i + v_h^s}{\varpi R} = \frac{v_h^i}{\varpi R} + \frac{v_h^s}{\varpi R} = \mu^i + \mu^s, \quad (4b)$$

where R is the rotor radius and ϖ is the speed of the rotor. The scalars λ^i , λ^s , separate the axial inflow ratio into induced and stream components, while the advance ratios μ^i and μ^s do the same for translational components of airflow. We also define the Lock number of a rotor as

$$\gamma = \frac{\rho C_{l_\alpha} c R^4}{\mathbb{I}_r}$$

where c is the rotor chord, C_{l_α} is the blade aerofoil lift curve slope, R is the radius of the rotor and moment of inertia \mathbb{I}_r .

Finally, we define the thrust, drag, and aerodynamic mechanical power coefficients as [21]

$$C_T := \frac{T}{\varpi^2}, \quad C_H := \frac{H}{\varpi^2}, \quad C_{P_{\text{am}}} := \frac{P_{\text{am}}}{\varpi^3}$$

respectively. Since ϖ varies over a large range for high-speed rotors typical of small multirotor vehicles, then working with

the aerodynamic coefficients C_T , C_H , and $C_{P_{\text{am}}}$ is better than working with the raw thrust and power when the key (18) and (19) are derived. In hover analysis, where $|\vec{v}^s| = 0$, then the C_T and $C_{P_{\text{am}}}$ coefficients are constant and one recovers the thrust and power models $T = C_T \varpi^2$ and $P_{\text{am}} = C_{P_{\text{am}}} \varpi^3$ used in existing RPM control systems. However, these relationships are only valid for static aerodynamic conditions and are invalidated the moment the hover condition is violated, in particular in the presence of updrafts or downdrafts [18]. By modeling the variation in C_T and $C_{P_{\text{am}}}$ in varying aerodynamic conditions and then measuring P_{am} and ϖ on the ESC, we will be able to reconstruct the aerodynamic condition of the rotor, compute C_T , and consequently compute the actual thrust T even in the presence of gusts. In hover, the drag coefficient $C_H = 0$ since there is no lateral movement of the rotor to create drag. If the rotor displaces air, then H and consequently C_H depends on the horizontal velocity of the rotor as noted in a range of previous works [1], [2], [22]. Modeling C_H is not a focus of this paper.

B. Momentum Theory

Momentum theory can be used to model the effects of the rotor aerodynamic power P_a in thrust generation. Using conservation of energy, mass, and momentum in the linear flow component within the streamtube and working with Glauert's assumptions on the streamtube [13], [18], the models for T , H , and aerodynamic power P_a including the correction for power lost in the wake modeled by the *induced power factor* κ , are given by [11], [12]

$$T = 2\rho A v_z^i |\vec{v}^a|, \quad (5)$$

$$H = 2\rho A v_h^i |\vec{v}^a|, \quad (6)$$

$$P_a = \kappa T v_z^i + T v_z^s + \kappa H v_h^i + H v_h^s \quad (7)$$

where ρ is the density of air and A is the area of the rotor disc. Note that (7) is simply a restatement of (2). In terms of the inflow ratios λ and μ (4), and thrust, drag, and power coefficients, then (5)–(7) can be rewritten as

$$C_T = 2\rho A R^2 \lambda^i \sqrt{\mu^2 + \lambda^2}, \quad (8)$$

$$C_H = 2\rho A R^2 \mu^i \sqrt{\mu^2 + \lambda^2}, \quad (9)$$

$$C_{P_a} = (\kappa C_T \lambda^i + C_T \lambda^s + \kappa C_H \mu^i + C_H \mu^s) R. \quad (10)$$

C. Blade Element Momentum Theory

Blade element theory considers individual elements of rotor blades and uses the classical aerodynamic theory of aerofoils to model the forces T , H , torque τ , and therefore aerodynamic mechanical power P_{am} of a rotor. *Blade element momentum theory* (BEMT) considers the blade geometry and aerodynamic properties (lift and drag) of the aerofoil in the aerodynamic conditions generated by the streamtube modeled using the momentum theory. Small fixed-pitch rotors designed for quadrotor vehicles are designed with approximately ideal pitch and ideal chord, i.e., the rotor pitches more steeply and increases in chord

length closer to the rotor hub in order to maintain the same lift properties in the changing aerodynamic condition caused by the slower linear velocity of the aerofoil element at closer radial stations along the blade. This design improves the hover performance of a rotor and also improves the validity of BEMT by allowing the rotor blade to operate at a similar angle of attack across the full length of the blade, with similar induced flow \vec{v}^i across the whole rotor disc. Although clearly this is a simplification of rotor aerodynamics, BEMT provides a robust yet relatively simple model that captures the key physical processes required for the approach proposed in this paper. We make the following assumptions.

Assumption 1: 1) The rotor blades are fixed pitch with near ideal twist and chord.

2) During axial motion, $|v_z^s|$ is such that it is less than or equal to the vertical induced velocity.

3) The flow is steady, irrotational, inviscid, incompressible, and locally 2-D.

The unsteady and irrotational components of flow are accounted for in the *induced power factor* κ . The assumption on $|v_z^s|$ ensures that during vertical ascent $(v_z^i + v_z^s) = v_z^a \geq 0$, $T \geq 0$ and no section of the blades is in the windmill state. The assumption on $|v_z^s|$ also ensures that during vertical descent, the flow is everywhere downward and the blades do not stall and thus maintain the linear lift model.

Since we model the thrust T along the rotor mast direction, we require a model for the blade flapping angle $\beta(\psi)$ in terms of rotor azimuth angle ψ , where $\psi \in [0, 2\pi]$. Given that the rotor blades on quadrotors are usually stiff, as such do not flap as much as full-scale helicopter blades, we model $\beta(\psi)$ using only the first two terms of a Fourier series harmonic model [12] with coefficients a_0 , a_1 , and b_1

$$\beta(\psi) = a_0 - a_1 \cos \psi - b_1 \sin \psi.$$

Let θ_0 denote the physical pitch angle of the blade and γ denotes the Lock number, then the model for these coefficients are given by [12]

$$a_0 = \frac{\gamma}{8} \left[\theta_0 (1 + \mu^2) - \frac{4}{3} \lambda \right],$$

$$a_1 = \frac{2\mu(4\theta_0/3 - \lambda)}{1 - \mu^2/2},$$

$$b_1 = \frac{\frac{4}{3}\mu a_0}{1 - \mu^2/2}.$$

Consider the rotor and a blade element shown in Fig. 4. The horizontal velocity component of the rotor blade at a radial distance r and azimuth angle ψ is given by

$$U_h(r, \psi) = \varpi r + (-V_h + W_h + v_h^i) \sin \psi.$$

For the vertical velocity $U_z(r, \psi)$

$$U_z(r, \psi) = v_z^i - V_z + W_z + r\dot{\beta}(\psi) + (-V_h + W_h + v_h^i) \times \beta(\psi) \cos \psi.$$

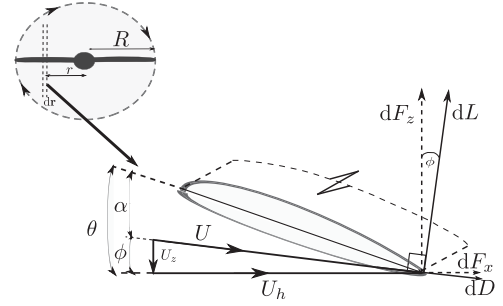


Fig. 4. Aerofoil section of a blade at a radial station $r \in [0, R]$ from the rotor hub. The figure shows the different elemental forces which include lift, drag, and the horizontal and vertical forces on the aerofoil in $\{C\}$. The flow angles and velocity components are also shown.

Normalizing or nondimensionalizing by dividing by the tip velocity of the rotor ϖR , the following relationships are obtained:

$$\begin{aligned} u_z(r, \psi) &= \frac{U_z(r, \psi)}{\varpi R}, \\ &= \lambda + \frac{r}{R\varpi} \dot{\beta}(\psi) + \frac{1}{R\varpi} \times (-V_h + W_h + v_h^i) \beta(\psi) \cos \psi, \\ &= \lambda + \frac{r}{R} \frac{d\beta(\psi)}{d\psi} + \mu \beta(\psi) \cos \psi \end{aligned}$$

and

$$\begin{aligned} u_h(r, \psi) &= \frac{U_h(r, \psi)}{\varpi R}, \\ &= \frac{r}{R} + \mu \sin \psi. \end{aligned}$$

The total or resultant velocity at the blade element is

$$|U(r, \psi)| = \sqrt{U_h(r, \psi)^2 + U_z(r, \psi)^2}.$$

For “slow” moving quadrotors with $|\vec{V}| < 5$ m/s, we assume $U^2(r, \psi) \approx U_h^2(r, \psi)$. This is a reasonable assumption given the much higher rotational tip speed of rotors used on quadrotors. For example, for a 10in diameter rotor blade (used on the quadrotor shown in Fig. 1), rotating at $\varpi \approx 5000$ RPM, then $U_h > 50$ m/s. Even if the entire velocity \vec{V} is in the vertical direction, $U_z \leq 5$ m/s and hence $U_z^2(r, \psi)$ is less than 1% of $U_h^2(r, \psi)$ and the approximation holds to well within the expected model error. Indeed, a 5% relative error would be acceptable, however 5 m/s disturbances are already toward the limit of the normal operating conditions, both in speed and expected updraft and downdraft disturbances expected for small quadrotor vehicles.

The elemental lift $dL(r, \psi)$ and drag $dD(r, \psi)$ forces expressed in $\{C\}$ are defined by

$$\begin{aligned} dL(r, \psi) &= \frac{1}{2} \rho U^2(r, \psi) C_l(r, \psi) c(r) dr, \\ dD(r, \psi) &= \frac{1}{2} \rho U^2(r, \psi) C_d(r, \psi) c(r) dr \end{aligned}$$

where C_l and C_d are the element lift and drag coefficients, respectively, and are given by

$$C_l(r, \psi) = C_{l_0} + C_{l\alpha}\alpha(r, \psi),$$

$$C_d(r, \psi) = C_{d_0} + KC_l^2(r, \psi), \quad K > 0.$$

$c(r)$ and $\alpha(r, \psi)$ are the element chord and angle of attack, respectively. The constants C_{l_0} , C_{d_0} , $C_{l\alpha}$, K are the zero-angle of attack lift coefficient, the zero-lift drag coefficient, the lift curve slope, and K a constant that depends on the blade planform geometry. From Fig. 4, the element angle of attack is defined by

$$\alpha(r, \psi) = \theta(r) - \phi(r, \psi)$$

where $\theta(r)$ is the blade section pitch and $\phi(r, \psi)$ is the relative inflow angle at the blade section. For $|\phi(r, \psi)| < 10^\circ$

$$\phi(r, \psi) \approx \tan^{-1} \left(\frac{U_z(r, \psi)}{U_h(r, \psi)} \right) \approx \frac{U_z(r, \psi)}{U_h(r, \psi)}.$$

A consequence of Assumption 1, however, is that the angle of attack $\alpha(r, \psi)$ is approximately constant along the entire blade length of the “near ideal” rotor [11]. The elemental forces in the \vec{e}_3 direction and in the horizontal plane $\text{span}\{\vec{e}_1, \vec{e}_2\}$ in $\{C\}$ are given by [12]

$$dF_x(r, \psi) = dL(r, \psi) \sin \phi(r, \psi) + dD(r, \psi) \cos \phi(r, \psi), \quad (11)$$

$$dF_z(r, \psi) = dL(r, \psi) \cos \phi(r, \psi) - dD(r, \psi) \sin \phi(r, \psi). \quad (12)$$

To obtain the models for T , H , and P_{am} for a “near ideal” rotor in steady state, we assume the rotor aerodynamic parameters $C_{l_0}(r, \psi) \approx 0$ and $KC_l^2(r, \psi) \approx 0$. In addition, applying Assumption 1 along with the definitions for the elemental forces ((11) and (12)), the forces can be resolved into T and H in $\{B\}$ thus the models can be derived for T , H , and P_{am} . Details of the derivations are found in Bangura *et al.* [11]. They are summarized in the following coefficient form:

$$C_T = \frac{1}{4} N_b \rho c_{\text{tip}} R^3 C_{l\alpha} (\theta_{\text{tip}}(2 + \mu^2) - 2\lambda), \quad (13)$$

$$C_H = \frac{1}{2} N_b \rho c_{\text{tip}} R^3 \mu \left[C_{d_0} + \frac{1}{2} X \right], \quad (14)$$

$$C_{P_{\text{am}}} = \frac{1}{4} \rho N_b c_{\text{tip}} R^4 C_{d_0} (2 + 5\mu^2) + (C_T(\kappa\lambda^i + \lambda^s) + C_H(\kappa\mu^i + \mu^s)) R \quad (15)$$

where

$$X = C_{l\alpha} \left(\theta_{\text{tip}}(\lambda - b_1 + \lambda a_0) + 2\lambda \left(4\frac{\theta_{\text{tip}}}{3} - \lambda \right) - 2\lambda b_1 \right).$$

The variable N_b denotes the number of blades, c_{tip} denotes the tip chord, and θ_{tip} denotes the tip pitch. It follows that BEMT along with the momentum theory analysis gives us the model of profile power P_p . Recalling (3) and noting that the second component of aerodynamic mechanical power P_{am} ($P_{\text{am}} = C_{P_{\text{am}}} \varpi^3$) in (15) which states explicitly that $C_{P_{\text{am}}} = C_{P_a} + C_{P_p}$, with the rotor aerodynamic power P_a ($P_a = C_{P_a} \varpi^3$) given by (10), then

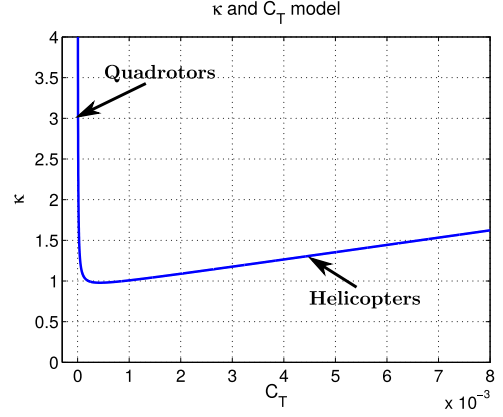


Fig. 5. Illustration of the induced power factor κ and thrust coefficient C_T for low- and high disc loading rotor blades, i.e., quadrotors and helicopters.

the profile power component of (15) is given by

$$P_p = \frac{1}{4} \rho N_b c_{\text{tip}} \varpi^3 R^4 C_{d_0} (2 + 5\mu^2). \quad (16)$$

D. Modeling the Induced Power Factor κ

Recall that κ models energy lost to nonuniform inflow, viscous drag, tip losses, wake swirl, and wake contraction. These effects are closely linked with the aerodynamic conditions generated by the rotor and their effect is much more significant on small rotor systems than full-scale helicopters. Their effects can be summarized into tip loss and rotor efficiency.

Define the disc loading of a rotor as

$$\text{DL} = \frac{T}{A}.$$

Note that the disc loading is closely related to the thrust coefficient through $\text{DL} = \frac{\varpi^2}{A} C_T$. Low DL rotors, that is, systems with large rotor areas relative to their generated thrust such as helicopters have high C_T but typically low-induced vertical velocity v_z^i and rotor speed ϖ . This makes them far more efficient in hover conditions than rotors with high disc loading. A dynamic increase in C_T is commonly associated with a decrease in λ^s , for example, an updraft will result in a $\lambda^s < 0$. Given the already high efficiency of such rotors any changes in λ^s will have a little effect on the aerodynamic efficiency of the rotor. However, changes in λ^s as a result of an updraft or downdraft will have a noticeable effect on the tip loss due to the increase or decrease in tip vortex generation. For high C_T , low DL rotors, the induced power factor κ is driven by tip loss and other parasitic drag effects. An increase in C_T results in a moderate increase in κ (see Fig. 5). This is the typical regime in which helicopters operate [18].

Small rotor systems for quadrotors, however, operate with very high disc loading and have correspondingly small thrust coefficients C_T while operating with relatively high ϖ . As such they operate with high vertical induced velocity v_z^i and are much less efficient (power efficiency ($\frac{T}{P_{\text{am}}}$)) than helicopter rotors. The presence of an updraft (increasing $-\lambda^s$) leads to an increase in C_T and a noticeable increase in aerodynamic efficiency. Such an updraft will also increase tip loss, however, the overall efficiency

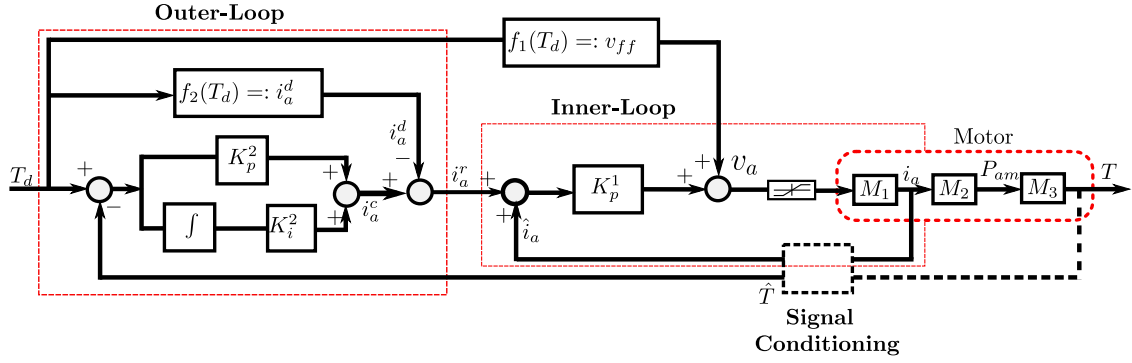


Fig. 6. Proposed thrust controller architecture showing the two control levels, controller gains, feedforward terms, signal conditioning, saturation block, and motor models M_1, M_2, M_3 . The controller runs at 1 kHz on the ESC [7]. The dotted thrust line indicates that thrust is estimated and not directly measured.

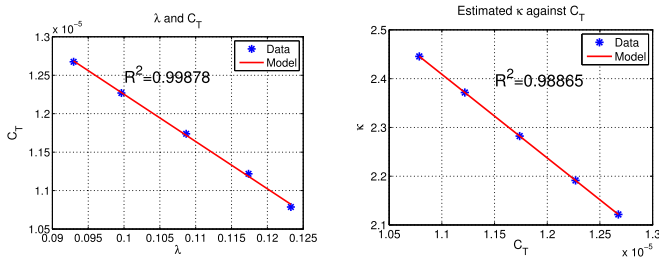


Fig. 7. Results for λ against C_T and C_T against estimated κ . The high R^2 values show good fit of the proposed models for the experimental data. Furthermore, the linear relationship between C_T and λ modeled by (18) is easily observable.

gain strongly dominates (see Fig. 5). Hence, for low C_T , high DL rotors, increasing C_T leads to a significant increase in rotor efficiency while losses due to tip loss are negligible thereby decreasing κ . This is the typical regime in which a quadrotor operates.

With reference to Fig. 5, we propose a general model for κ to be

$$\kappa = \text{const.} + \text{const.} C_T + \text{const.} \frac{1}{C_T}$$

where we do not provide symbols for the positive constants for the moment. Fig. 5 graphs κ versus C_T for low disc loading (helicopters) and high disc loading (quadrotor) rotors, the rotor system used for the experimental work in this paper and based on values obtained in Section IV. For the rotors on our quadrotor vehicle where $C_T \ll 10^{-4}$, the dominant part of the model is the hyperbolic term $1/C_T$. This is supported by experimental results shown in Fig. 7 of Section IV. Note that the model plotted in Fig. 5 is supported by [18, Figure 3.18, pg. 105], although the nature of the high disc loading model is not considered by Leishman as it is not relevant to the helicopter rotors discussed [18].

In practice, the rotor for our vehicle will never function outside of the dominant region where $0 < C_T \ll 10^{-3}$. In this region, the linear term $\text{const.} C_T$ is negligible, while the hyperbolic term can be approximated by a linear function

$$\frac{1}{C_T} \approx \frac{\text{const.}}{\bar{C}_T} - \frac{\text{const.}}{\bar{C}_T^2} (C_T - \bar{C}_T)$$

where \bar{C}_T is an operating point. Thus, it is sufficient to approximate the κ model by a linear model in the region of operation of such rotors by

$$\kappa = d_0 + d_1 C_T \quad (17)$$

where $d_0 > 0$ is a positive constant and $d_1 < 0$ is a large and negative constant. Using a linear model of this nature reduces the computational burden on the already heavily loaded embedded microcontroller on the ESC.

E. Thrust Computation

The variables in (13)–(15) are $C_{P_{am}}, C_T, C_H, \mu^i, \mu^s, \lambda^i, \lambda^s, \kappa$, and ϖ . At the local ESC level, it is possible to measure ϖ directly and estimate P_{am} and therefore $C_{P_{am}}$ by measuring the electrical power into the motor and compensating for electrical losses (see Section III-A) [7]. Thus, we have seven unknowns $C_T, C_H, \mu^i, \mu^s, \lambda^i, \lambda^s, \kappa$ and four constraint equations ((13), (14), (15), and (17)).

A number of authors have noted that the horizontal velocities v_h^s, v_h^i , force H and therefore μ^s, μ^i, C_H are related to the horizontal acceleration of the vehicle [1], [2], [22] and can be measured using the accelerometers in an IMU. Using such measurements, it should be possible to resolve the remaining four unknown variables from the algebraic constraints ((13), (15), and (17)). Although this appears to be a promising approach, the ESC on a typical quadrotor is not equipped with an accelerometer and the communication link to the central IMU is far lower bandwidth (typically 50 Hz) than the ESC control loop operational frequency (typically 1–2 kHz), making corrections for horizontal aerodynamics difficult.

Rather than take such an approach, we argue that the contribution of the horizontal variables to the aerodynamics of the rotor is effectively negligible for most aerial robotics applications and can be ignored. Considering (13) and (15), we note that the μ variable appears as a quadratic μ^2 . For quadrotors in near hover conditions, typical of many robotic applications, the advance ratio μ is naturally small and consequently its square is negligible. Furthermore, with v_h^s small, consequently v_h^i is also small, such that the term $C_H (\mu^s + \kappa \mu^i) \propto \mu^2$ and can thus be ignored. Formally, we make the following assumption.

Assumption 2: The advance ratio μ is small, such that $\mu^2 \approx 0$ within the accuracy of the aerodynamic model.

CFDs results on translational flight presented in [19] showed that for translational velocities up to $V_h = 10$ m/s, the total power gained by all four rotors is only 6%. This validates our decision to ignore the effect of translational lift for typical robotics applications. This assumption decouples the dependence of (14) with (13) and (15). The horizontal components of force C_H , and velocity ratios μ^i and μ^s no longer contribute to the vertical aerodynamics in (13) and (15). This leaves four aerodynamic variables C_T , λ^s , λ^i , and κ along with three constraint equations (13), (15), and (17). The final constraint is provided by the expression for C_T derived from the momentum theory (8). To simplify the notation in the sequel, we define lumped coefficients

$$c_0 = R, \quad c_1 = \frac{1}{2} N_b \rho c_{\text{tip}} R^3 C_{l\alpha},$$

$$c_2 = \theta_{\text{tip}}, \quad c_3 = \frac{1}{2} \rho c_{\text{tip}} N_b C_{d0} R^4.$$

From Assumption 2, (13) and (15) can be rewritten respectively as

$$C_T = c_1 [c_2 - \lambda], \quad (18)$$

$$C_{P_{\text{am}}} = c_3 + C_T (\kappa \lambda^i + \lambda^s) c_0. \quad (19)$$

Recalling from Assumption 2 that $\mu^2 \approx 0$, then (8) becomes

$$C_T = c_4 \lambda^i \lambda \quad (20)$$

where $c_4 = 2\rho A R^2 = 2\rho A c_0^2$.

The relationship (20) along with (18) provides a constraint between λ^i and λ^s . It is convenient to make this relationship explicit rather than work with the two separate constraints. Equating (20) to (18) and collecting terms yields

$$c_4 (\lambda^i)^2 + \lambda^i (c_4 \lambda^s + c_1) + c_1 (\lambda^s - c_2) = 0. \quad (21)$$

In summary, one has aerodynamic variables C_T , λ^s , λ^i , and κ , constraint equations (17)–(20), depending on aerodynamic coefficients d_0 , d_1 and c_0 , c_1 , c_2 , c_3 , and c_4 . The aerodynamic coefficients are determined offline using linear regression described in Section IV-B.

The proposed iterative scheme for solving (17), (18), (19), and (21) (implemented as described in Section V) is outlined in Algorithm 1. The approach taken is tailored to exploit the fact that once the stream inflow ratio λ^s is known, it is straightforward to compute C_T , κ , and $C_{P_{\text{am}}}$ sequentially, but difficult to compute a single function of all variables. We generate two initial estimates λ_1^s and λ_2^s based on the previous estimate λ^s and a small offset Δ of the previous estimate. Then, for each estimate λ_k^s , we compute the aerodynamic variables one-by-one. We define an implicit function

$$f(\lambda^s) = C_{P_{\text{am}}}(t) - C_{P_{\text{am}}}$$

where $C_{P_{\text{am}}}$ is the computed value based on the guess of λ^s and $C_{P_{\text{am}}}(t)$ is the measured value at time t . The goal is to find λ^s that makes $f(\lambda^s) = 0$. The two initial guesses λ_1^s and λ_2^s form the first two elements of a Newton–Secant iteration

Algorithm 1: Thrust Computation.

```

1: Data  $c_0, c_1, c_2, c_3, c_4, d_0, d_1, N, \Delta, \epsilon$ .
2: Local state  $\text{old}[\lambda_k^s]$ .
3: For each measurement  $C_{P_{\text{am}}}(t) = \frac{\dot{P}_{\text{am}}}{\omega^3}$  at time  $t$ .
4: Set  $k = 1$ ; Set  $\lambda_1^s = \text{old}[\lambda_k^s] - \Delta$ 
5: for  $k = 1 \dots N$  do
6:   if  $k = 2$  then; Set  $\lambda_2^s = \text{old}[\lambda_k^s]$ ;
7:   Use (21) to compute  $\lambda^i$ ;
8:   Use (18) to compute  $C_T$ ;
9:   Use (17) to compute  $\kappa$ ;
10:  Use (21) and (19) to compute  $C_{P_{\text{am}}}$ ;
11:  Compute  $f(\lambda_k^s) = C_{P_{\text{am}}}(t) - C_{P_{\text{am}}}$ ;
12:  if  $k > 2$  and  $|f(\lambda_k^s) - f(\lambda_{k-1}^s)| < \epsilon$  then break
13:  Compute  $\lambda_{k+1}^s = \lambda_k^s - f(\lambda_k^s) \frac{\lambda_k^s - \lambda_{k-1}^s}{f(\lambda_k^s) - f(\lambda_{k-1}^s)}$ ; return
14: Set  $\text{old}[\lambda_k^s] = \lambda_k^s$ ;
15: Output  $T = C_T \omega^2$ ;

```

that converges to the optimum λ^s . A simple stopping criteria based on decrease in $f(\lambda_k^s)$ with a precision ϵ is used to exit the loop. In practice, the loop usually converges in three–four iterations (that includes the two initialization values) and rarely runs more than five iterations. The arbitrary limit $N > 3$ on total iterations of the for loop ensures that the code meets run time requirements—although we use $N = 20$, in practice and have never seen the for loop run to completion.

III. THRUST CONTROL DESIGN

In this section, we propose a hierarchical controller for thrust regulation based on the aerodynamic theory and thrust computation scheme developed in Section II along with the electromechanical properties of the motor–rotor system.

The proposed control architecture for the regulation of thrust is shown in Fig. 6. It consists of a cascaded control structure with an inner current control loop, and an outer thrust regulation loop. The inner loop is a positive proportional-feedforward controller and the outer thrust control loop is a PI control with feedforward. Together, this simple architecture effectively regulates the thrust of the rotor at minimal complexity and fast transient response.

A. Motor Model and Power Estimation

If v_a, i_a are the voltage and current through a motor and ω is the speed of the rotor, the model for a brushless direct current motor is given by [7]

$$v_a = K_e \omega + i_a R_a + L_a \frac{di_a}{dt}, \quad (22a)$$

$$\tau = (K_{q0} - K_{q1} i_a) i_a, \quad (22b)$$

$$\mathbb{I}_r \dot{\omega} = \tau - \tau_D \quad (22c)$$

where R_a is the motor resistance, K_e is a constant that is related to the K_v (where $\omega = K_v v_a$) rating of the motor, and L_a the motor coil inductance. The constants K_{q0} and K_{q1} are the current to torque (τ) constants. The quadratic term $K_{q1} i_a^2$ in (22b) accounts for the degrading torque efficiency associated

with high currents [7] and \mathbb{I}_r is the rotor moment of inertia and τ_D is the torque as a result of the rotor aerodynamic drag. The power associated with accelerating or decelerating the rotor is given by

$$P_r = \mathbb{I}_r \dot{\omega} \dot{\omega}.$$

The full mechanical power supplied to the rotor through the rotor mast is given by

$$P_m = \tau \dot{\omega}. \quad (23)$$

The power balance for the rotor mast can be written as

$$P_{am} = P_m - P_r \quad (24)$$

where P_{am} is the aerodynamic mechanical power derived in Section II-C. A suitable ESC provides direct measurements of $\dot{\omega}$, i_a , and v_a . Measurements of these quantities are noisy and to obtain usable data for estimation and control, it is important to filter and condition the signals. A set of complementary filters based on (22a) and (22b) were proposed by Bangura *et al.* [7]. These filters achieve reasonable signal conditioning \hat{i}_a and \hat{v}_a of the raw measurements and also provide an estimate $\hat{\dot{\omega}}$ of $\dot{\omega}$. The raw measurements of $\dot{\omega}$ do not require filtering.

An estimate of the aerodynamic mechanical power input into the air \hat{P}_{am} can now be computed directly from the measured and estimated variables

$$\hat{P}_{am} = (K_{q0} - K_{q1} \hat{i}_a) \hat{i}_a \hat{\dot{\omega}} - \mathbb{I}_r \hat{\dot{\omega}} \hat{\dot{\omega}}. \quad (25)$$

Once power has been estimated, it is used in the computation of thrust as described in Section II. This thrust is then regulated using the outer-inner loop controllers shown in Fig. 6 directly on the ESC.

B. Control Design

The proposed hierarchical controller for regulation of thrust is shown in Fig. 6. In the motor model, M_1 is a combination of (22a) and (22c) to model the nonlinear model between v_a and i_a . M_2 is the nonlinear model that relates i_a and the aerodynamic mechanical power P_{am} and M_3 represents the nonlinear model that maps P_{am} to T as outlined in Section II-E.

The low-level current controller is crucial in generating fast $\dot{\omega}$ response using high gain inner-loop control, hence avoiding the need for exceptionally high gains in the outer loop where noise in the estimated feedback signals would be a problem. The low-level current controller is defined by

$$v_a = v_{ff}(T_d) + K_p^1 (\dot{i}_a^r + \hat{i}_a) \quad (26)$$

where $v_{ff}(T_d)$ is a feedforward voltage, \hat{i}_a is the measured current, $\dot{i}_a^r = \dot{i}_a^c - \dot{i}_a^d$ is the reference control current; comprising the control current \dot{i}_a^c from the outer-loop PI controller minus the “desired” feedforward current \dot{i}_a^d , see Fig. 6. We propose a positive (unstable) inner-loop feedback, the $+i_a$ term, in the control design which in turn dictates a negative feedforward term $-i_a^d$, with the feedthrough control term $+i_a^c$ positive as is usual. The use of positive inner-loop feedback is a key aspect of the control design and is important in generating the desired rise

time of the full system. To understand the role of the gain, consider the linearization of the inner-loop current control around some fixed constant thrust condition. The following model is derived in Appendix A:

$$H_1(s) = \frac{\dot{i}_a}{v_a} = \frac{K_p^1 [K_e K_q + R_a (\mathbb{I}_r s + \delta)]}{\mathbb{I}_r s + \delta - K_p^1 [K_e K_q + R_a (\mathbb{I}_r s + \delta)]}$$

where δ is a damping factor associated with the linearization of the aerodynamic damping [7] and $K_q = (K_{q0} - 2K_{q1} \dot{i}_a^*)$ is defined in Appendix A. By choosing $K_p^1 > 0$ suitably, the poles of this transfer function can then be placed close to the imaginary axis but remain stable, ensuring fast rise time with very high overshoot of the current response. A large overshoot in the current response provides the surge of power necessary to spin up (or spin down) the rotor. In order to prevent overcurrent, the computed voltage is saturated based on the maximum current through the ESC and instantaneous $\dot{\omega}$ measurement using (22a). Since the actual control design is a pure proportional control and the inherent current dynamics are stable, saturation will not destabilize the system. The stability bound $K_p^1 \leq \frac{\delta}{K_e K_q + R_a \delta}$ (32), Appendix A, ensures that the poles will remain stable. The parameters in this bound are relatively easy to determine (see Section IV-A) from the electric motor parameters of a motor-rotor assembly and tuning K_p^1 is straightforward.

In the outer loop, governing actual thrust control, we propose a feedforward and PI feedback controller. The feedback controller design of this system is a straightforward linear design once the inner control loop is stabilized. The overall control architecture includes only a single integrator at the outer level to avoid dynamic complexity. The feedforward terms are included to limit the offsets associated with the simple proportional gains in the control architecture.

The feedforward terms are obtained by considering steady-state hover and static-free air conditions ($|\vec{v}^s| = 0$). The feedforward term $f_1(T_d)$ is derived from (22a). From the voltage equation, $\frac{1}{K_e^2} (v_a - i_a R_a)^2 = \dot{\omega}^2$, hence

$$T_d = \frac{C_T}{K_e^2} (v_a - i_a R_a)^2.$$

Thus, a quadratic model for $f_1(T_d)$ derived above is used.

To obtain $f_2(T_d)$, consider the electrical torque ($\tau = K_q \dot{i}_a$) and aerodynamic ($\tau_D = C_Q \dot{\omega}^2$) torque at steady state (i.e., $\dot{\omega} = 0$), where C_Q is the torque coefficient. Hence, $\dot{i}_a = \frac{C_Q}{K_q} \dot{\omega}^2$. From this, it is easily seen that $T_d = C_T \frac{K_q}{C_Q} \dot{i}_a$, hence, a linear function relating T_d and \dot{i}_a is obtained for $f_2(T_d)$.

IV. LABORATORY CALIBRATION

In this section, we outline calibration procedures used for the proposed thrust estimation and control scheme presented in Sections II and III. There are two calibration procedures: motor/electrical and rotor/aerodynamic. The procedures require measurements of v_a , i_a , $\dot{\omega}$ provided by the ESC [5], force, and torque by a six-axis force-torque sensor [29] and the axial stream velocity v_z^s read from a hand-held anemometer. The calibration results presented may appear to have large errors in

many of the parameters. It is important to recall however, that the predictive power of (17)–(20) is more important than the actual values of the coefficients. We demonstrate this through the ANOVA analysis of the model fit. Although the calibration described in this section depends on laboratory facilities, we believe that field calibration procedures can be developed, however, such a study is beyond the scope of this work.

A. Motor Calibration

This involves determining the electrical constants (K_e , R_a , L_a) outlined in Section III-A which are necessary for the implementation of the filters in [7]. With steady-state measurements of v_a , i_a , and ϖ , applying linear regression to (22a), the constants K_e and R_a are determined. With K_e and R_a determined, the transient data to the different steady states can be used to determine L_a . In addition, to obtain K_{q0} and K_{q1} , the torque (τ) measurements provided by the force–torque sensor are used in a second regression based on (22b). Results of these regressions are available in [7].

B. Aerodynamic Calibration

The goal of the aerodynamic calibration is to determine the aerodynamic coefficients c_0 , c_1 , c_2 , c_3 , and d_0 , d_1 . The available measurements are power P_{am} and rotor RPM ϖ from the ESC, thrust T from the force–torque sensor. The power coefficients $C_{P_{\text{am}}}$ and C_T can be determined algebraically from this data. Since $C_{P_{\text{am}}}$ and C_T are constant at hover condition, it is necessary to generate nonhover conditions to observe the underlying aerodynamic constants. The most direct way in which to achieve this is by placing the rotor in a controlled wind environment. A crude laminar flow generator for generating v_z^s is used and the motor–rotor system is mounted on a force–torque sensor shown in Fig. 8. Note that the motor–rotor assembly is inverted ensuring that the external flow is adding to the induced velocity (increased λ) rather than opposing, a more robust experimental configuration that avoids complex stream effects seen in descending rotor aerodynamics.

The aerodynamic coefficient c_3 can be determined with a single standalone experiment. The rotor is fixed at a range of RPM and then the velocity of the wind $|v_z^s|$ is adjusted until the average thrust is zero; that is, $C_T = 0$. There is still a residual torque associated with the operation of the blade and this is associated with the constant c_3 (19). We performed a set of nine experiments with each experiment running for 70 s. The resulting estimate for c_3 was

$$c_3 = 1.2998 \times 10^{-8} \pm 2.355 \times 10^{-8}. \quad (27)$$

The next stage is to determine c_0 , c_4 , d_0 , and d_1 the coefficients associated with the momentum theory model and the induced power factor κ using (19) and (20) that are independent of c_1 and c_2 . The parameter $c_0 = R$ is nominally the radius of the rotor. However, this parameter is primarily associated with characterizing the cross-sectional area of the stream tube in the momentum theory derivation and this depends on the effective operation of the rotors. All rotorcrafts suffer from some effective decrease of the rotor radius due to tip loss and other effects.

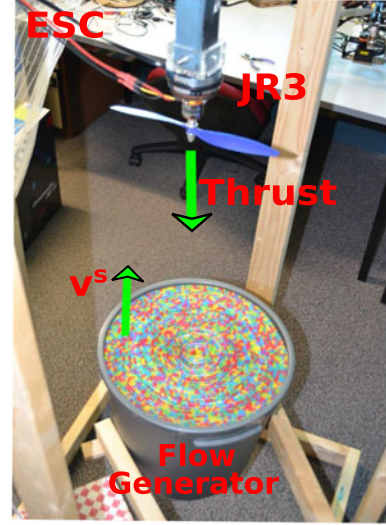


Fig. 8. Experimental setup for calibration and the static downdraft experiments. The rotor is inverted for simplicity and a downdraft condition is generated by the ascending wind. The laminar flow generator is fabricated from 10cm long sections of coloured drinking straws glued into the top of the plastic bin in which a 10in propeller is controlled to generate constant stream velocity \vec{v}^s directed in the axial direction. The velocity of the air is hand measured using an anemometer. The experimental motor–rotor system is mounted on a force–torque sensor and connected to an isolated ESC. The isolated ESC has the RPM and proposed scheme implemented to control the desired thrust force setpoint T .

However, all quadrotor rotor blades have significant tip and root cutouts and their effective radius is significantly less than the Prandtl estimate. To account for this reduction, we will estimate c_0 as well as the other aerodynamic coefficients.

We will estimate the aerodynamic parameters by undertaking a sequence of coupled regressions. The parameters identified in each stage are denoted $c_0(k)$, $c_4(k)$, $d_0(k)$, and $d_1(k)$ for $k = 1, 2, \dots$. For the initial stage, we assume $c_0(1) = R$ the rotor radius and this leads to an estimate $c_4(1) = 2\rho\pi c_0^2$. Using measurements of thrust T , λ^s , and ϖ and using (20), the following relationships are used to obtain λ^i and λ

$$\lambda^i = \frac{-\lambda^s + \sqrt{(\lambda^s)^2 + \frac{4C_T}{c_4}}}{2},$$

$$\lambda = \lambda^i + \lambda^s.$$

Now using (19) along with the estimate for c_3 (27), one has

$$C_{P_{\text{am}}} - c_3 = c_0(k)C_T\lambda^s + C_T\lambda^i d_0(k)c_0(k) + C_T^2\lambda^i d_1(k)c_0(k). \quad (28)$$

A regression on this equation yields values for $c_0(2)$, $d_0(2)c_0(2)$, and $d_1(2)c_0(2)$. The value for $c_0(2)$ is now used to generate a new $c_4(2)$ and the λ^i and λ variables are recomputed. The regression on (28) can be run using the new inflow ratios and the whole process is iterated (by hand by an available Ph.D. student) until the values converge. Performing this process, one obtains the results summarized in Table I. From the regression, we obtain an effective radius $c_0 = 0.57R$, that is, 57% of the physical rotor radius R . This might appear low, however, considering the quality of the construction of such cheap blades

TABLE I
ESTIMATED AERODYNAMIC COEFFICIENTS USING LINEAR REGRESSION

Parameter	Estimate	95% Confidence Interval
c_1	6.1490×10^{-5}	$[5.7215 \ 6.5242] \times 10^{-5}$
c_2	0.2993	[0.2883 0.3135]
c_3	1.2998×10^{-8}	$[-1.0552 \ 3.6548] \times 10^{-8}$
d_0	4.2959	[-3.0642 11.7926]
d_1	-1.7154×10^5	$[-6.7367 \ 3.2139] \times 10^5$
c_0	0.0724	[0.0637 0.0811]

TABLE II
ANALYSIS OF VARIANCE (ANOVA) FOR THE SEPARATE REGRESSIONS

$C_{P_{am}} - c_3 = c_{0e} C_T \lambda^s + C_T (d_0 + d_1 C_T) \lambda^i c_{0e}$			
Source	SumSq	DF	MeanSq
Corrected Total	4.9306×10^{-15}	4	1.2326×10^{-15}
Model	4.9288×10^{-15}	2	2.4644×10^{-15}
Error	1.805×10^{-18}	2	9.0251×10^{-19}
$C_T = c_1 c_2 - c_1 \lambda$			
Source	SumSq	DF	MeanSq
Corrected Total	2.3187×10^{-12}	4	5.7967×10^{-13}
Model	2.3157×10^{-12}	1	2.3157×10^{-12}
Error	2.9474×10^{-15}	3	9.8246×10^{-16}

with significant root cutout, it is not surprising that the effective cross-sectional area that is appropriate for momentum theory is quite small.

Remark 3: It is not possible to identify c_3 in the same process as c_0 , c_4 , d_0 , and d_1 since both processes separately model dissipation losses in the rotor model.

Finally, we use (18) to identify parameters c_1 and c_2 . This is a straightforward regression on the lumped parameters $c_1 c_2$ and c_1 . The results of this regression are also summarized in Table I.

Due to the different units for the various aerodynamic parameters, it is important to use preconditioning on the data to avoid ill conditioning in various regressions. We use a preconditioner based on the magnitude of entries in the regression vector. The limitations of the experimental system available meant that we only collected $N = 5$ data points for $v_z^s = (0.0, 1.5, 2.3, 3.3, 4.2)$ m/s and the associated C_T , $C_{P_{am}}$, λ^i , λ^s . This limitation in data leads to the large 95% confidence intervals for the parameter estimates as recorded in Table I. However, the key requirement for the performance of the model is not individual parameter estimates, but rather the accuracy of the model. We demonstrate this first in Fig. 7. Here, we have plotted the projected regressions for λ versus C_T , which corresponds to (18), and C_T versus κ which corresponds to (17). In particular, the increase in efficiency (decrease in κ) with increase in C_T is clearly visible.

To check the accuracy of the C_T (18) and $C_{P_{am}}$ (19) models, we performed an *analysis of variance* ANOVA analysis of residuals. The results of this analysis is displayed in Table II for the DF, the sum of squares, and mean square error. The obtained sum of squares and the mean sum of squares are several orders of magnitude less than $(C_T)^2$ and $(C_{P_{am}})^2$. Table III shows the

TABLE III
FURTHER ANOVA RESULTS FOR THE C_T AND $C_{P_{am}}$ MODELS

Model	Adjusted R^2	RMSE
$C_{P_{am}}$	0.999	9.5×10^{-10}
C_T	0.998	3.13×10^{-8}
$C_{P_{am}} - c_3 = c_{0e} C_T \lambda^s + C_T (d_0 + d_1 C_T) \lambda^i c_{0e}$		
$C_T = c_1 c_2 - c_1 \lambda$		

adjusted R^2 which are almost unity implying that the models explain the experimental data to a high level of accuracy. Furthermore, the *root mean square error* (RMSE) for both models have magnitude of orders of magnitude smaller than the model parameters of the regression thus providing further evidence on the accuracy of the model.

Carrying out regression on the following pairs of data: (T, v_a) , (T, i_a) , to determine the parameters for $f_1(T_d)$ and $f_2(T_d)$ is a straightforward process.

V. EXPERIMENTAL RESULTS

In this section, we present both static experimental and dynamic flight test results to evaluate the performance of the proposed thrust controller. Experimental results for a state-of-the-art rotor RPM (ϖ) controller are also provided to provide a comparison. The section starts by describing the current static thrust model and RPM controller.

A. Classical RPM Rotor Control

The classical model for thrust is based on a static-free air model that relates thrust T to rotor speed ϖ and is given by [21]–[23], [26]

$$T = C_T \varpi^2.$$

The inadequacy of this model in modeling actual thrust generated leads to the proposition of a modified model to obtain a good fit for thrust and ϖ . The thrust to RPM model that is currently the accepted standard in the literature is [5], [8], [10]

$$T = C_{T0} \varpi + C_T \varpi^2 \quad (29)$$

where C_{T0} and C_T are constants determined from static tests. For the rotors used on our quadrotor, with ϖ measured in RPM and T in N, the coefficients obtained through regression are $C_T = 1.9 \times 10^{-7}$, $C_{T0} = -1.77 \times 10^{-4}$. The C_{T0} term is added in particular to improve the thrust model at lower rotor speeds. Operating at an RPM of approximately 4500, the effect of the linear correction term is small but still important.

For a desired thrust T_d , the desired ϖ_d is determined using (29). The desired rotor speed ϖ_d is then controlled using a feedforward voltage along with a PI feedback controller given by [5], [10]

$$v_a = v_{ff}(\varpi_d) - K_p(\varpi - \varpi_d) - K_i \int_0^t (\varpi - \varpi_d) dt \quad (30)$$

where $K_p, K_i > 0$ are the feedback gains and $v_{ff}(\varpi_d)$ is the feedforward voltage.

TABLE IV
SUMMARY OF STATIC TEST RESULTS FOR MEAN VARIATIONS
OF THRUST FROM A DESIRED VALUE $T_0 = 3.2\text{N}$ AND THEIR 1σ
VARIATIONS AS PERCENTAGES $\left(\frac{T-T_0}{T_0} \%\right)$

v_z^s (m/s)	RPM Controller	New Controller
0	0 ± 0.2324	0 ± 3.4257
0.8	-1.9897 ± 2.2923	0.0328 ± 3.6745
2.2	-10.4906 ± 3.2013	0.0342 ± 3.4153
3.5	-13.7860 ± 1.9289	0.0078 ± 3.4075
3.8	-15.8434 ± 2.5288	-4.5829 ± 3.4298
4.0	-18.6991 ± 3.7215	-0.0931 ± 3.3447
4.2	-20.7216 ± 0.6022	-1.8781 ± 2.8694

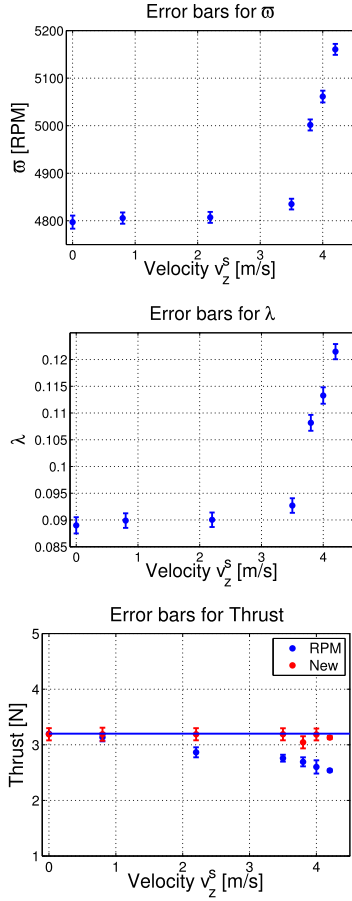


Fig. 9. The figure shows mean variations and 1σ error bars in ω and λ resulting from using the new scheme and controller to producing a desired thrust of 3.2N in downdrafts (v_z^s) of varying strengths. It is these dynamic changes in ω and computed λ at the local ESC level that enable the computation and control of thrust to the desired physical value. The third plot shows the measured thrust and error bars for 1σ variation in the measured mean thrust per experiment for the different downdraft strengths resulting from the two controllers thus confirming that we are able to maintain an almost constant desired thrust with the new scheme in the varying aerodynamic conditions.

In summary, the coefficients $C_{T0}, C_T, v_{ff}(\omega_d)$ are experimentally determined using a force sensor and ESC measurements of ω and v_a and then the gains K_p, K_i are tuned in static ($|\vec{v}^s| = 0$) free-air conditions. The voltage v_a determined from the proposed controller of (26) and that of (30) are implemented on the ESC as a *pulse width modulation* of the bus voltage.



Fig. 10. Comparison of the transient responses of the current state-of-the-art RPM-based model and controller to the new scheme and controller to step input in thrust. The filtered force measurements are provided by the JR3 force-torque sensor. The results show similar transient characteristics of both controllers.

B. Static Rotor Experiments

The aim of the static rotor experiments is to demonstrate the improvements of the proposed scheme and controller compared to desired RPM control for regulating thrust to a desired setpoint in the presence of downdrafts of varying strengths. The experimental setup is shown in Fig. 8 and consists of a six-axis force-torque sensor [29], an anemometer, a custom-made laminar flow generator to provide controllable wind conditions and an ESC equipped with both the RPM and new controllers.

The experiment is undertaken by adjusting the flow generator until the desired stream velocity is attained. Then, the control on the motor-rotor is initiated at the desired thrust setpoint and, after the transient has died out, data are collected from the force sensor for a period of 60 s. The data are averaged to obtain the results shown below. A summary of the mean variation of thrust measured by the force-torque sensor from the desired thrust setpoint ($T = 3.2\text{N}$) when both controllers are subject to downdrafts of varying strengths is presented in Table IV.

From these results, it is clear that the new controller outperforms the current state-of-the-art RPM controller in maintaining the desired thrust setpoint in varying strengths of downdrafts. Fig. 9 shows the resulting variations in ω and the vertical inflow ratio λ in maintaining the desired thrust setpoint T by the new scheme. The changes in λ correspond to changes in the strength of the downdrafts. These λ changes correspond to changes in C_T given by (18) and therefore thrust. In order to produce the desired thrust, the new controller changes the desired aerodynamic mechanical power P_{am}^d which in turn changes the desired ω . Computed λ and the corresponding ω along with 1σ variations in the mean of a set of subexperiments using the new scheme and controller are shown as error bars in Fig. 9. The measured thrust by the force-torque sensor along with 1σ variations in the mean are also shown to verify that the desired thrust is maintained irrespective of changing v_z^s . Just as predicted, the RPM scheme and controller is unable to maintain the desired thrust and becomes less effective with increasing values of v_z^s .

C. Transient Response

A key requirement of motor-rotor control is to obtain good transient response for the rotor. Based on the stability bounds

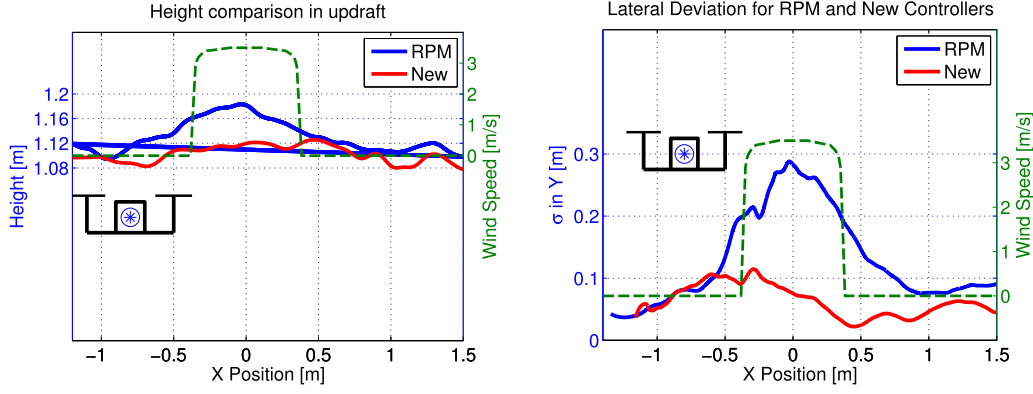


Fig. 11. Comparison of the RPM and the proposed controllers for position/trajectory control. Data presented are taken over an average of 50 flights per controller. The figures compare the heights and the standard deviations in the lateral y -direction for both the RPM and new controllers. The quadrotor is made to fly across a room at a desired $V_x = -0.3$ m/s, $V_z = 0$, height = 1.1 m, $V_y = y = 0$ in the presence of a gust generator centred at $(0, 0, 0)$ with distribution shown in green on both figures. A scaled graphic of the quadrotor with centre of mass indicated by \otimes is superimposed on both figures to provide an indication of when the front rotor encounters the flow region when it is at a distance 0.8 m away from the centre of the gust. The deviation of the quadrotor from its desired trajectory is clear for the RPM controller while for the proposed thrust controller the deviation is minimal.

on (32) of our proposed scheme, the choice of K_p^1 that gives a high stable overshoot with damping factor less than 0.1 of the current dynamics is $K_p^1 = 0.01$. To verify that the proposed scheme has a good transient response, a series of step responses were undertaken for which one set of results is shown in Fig. 10. Both the RPM and new controller were tuned to obtain the best transient that we could achieve. The transient response of both control architectures are in the order of 50 ms rise time. This transient response is constrained by the physical limitations of the system, primarily current saturation, and the rise-time is the best that can be achieved with this hardware. Both motor-rotor controllers contain integral terms and will have zero steady-state tracking error up to the limit of the thrust model. In this case, since the stream velocity $\vec{v}^s = 0$, the RPM thrust model should be accurate and the steady-state response of both schemes is expected to be the same. Circulation of wind in the laboratory will cause gusts that lead to thrust variation.

D. Flight Tests

To evaluate the effectiveness of the proposed approach in free flight, we perform a constant velocity flight ($V_x = -0.3$ m/s) at a constant height ($z = -1.1$ m) using the *proportional derivative* position and trajectory tracking controllers presented in [8] for both the proposed thrust control and controllers. The transient responses of the two motor-rotor controllers are quantitatively equivalent as shown in Fig. 10 and the same outer-loop controller is used. It is reasonable to expect that any qualitative difference in the performance of the closed-loop flight system will be due to sensitivity of the motor-rotor response to unmodeled aerodynamic effects in the thrust model rather than any fundamental difference in the control design.

To excite the gust response of the vehicle, the trajectory was chosen to fly directly over the “almost laminar” flow generator of radius 0.35 m located in the middle of the flying space and blowing with a vertical wind of strength $v_z^s = 3.5$ m/s. This is a strong gust disturbance for the small quadrotor vehicle used as the experimental platform. The results for the RPM-based

scheme and the proposed method are shown in Fig. 11 and the accompanying video.

To interpret the trajectories shown in Fig. 11, it is important to realize that the gust is not applied evenly to the vehicle. During forward motion, the tip of the front blade touches the updraft when the centre of mass of the vehicle represented by \otimes is roughly 0.8 m (arm length of the vehicle is 0.3 m, blade radius $c_0 = 0.127$ m, and radius of updraft is 0.35 m) from the centre of the updraft. With the RPM controller, the updraft induces a strong upward pitching motion that directs the centre of the quadrotor (\otimes) toward an upward trajectory, even though at this time the centre of the quadrotor is still some distance from the gust. Moreover, as the vehicle crosses the gust, the front rotor exits first, and the vehicle descends even while the rear rotor is still in the gust. In contrast to the RPM control, the thrust control algorithm is not significantly affected by the gust and the quadrotor trajectory is not significantly disturbed.

It is interesting to note that the lateral deviation of the vehicle is even more extreme than vertical divergence. This is due to the instability of the two opposing air columns interacting with each other. The destabilization of the air column interaction causes strong roll (and pitch) disturbances and lead to the vehicle veering strongly off course. This effect is most significant during the entry phase as the quadrotor is being forced to ascend and the controller is fighting against the updraft. As the front rotor exits the flow region, the quadrotor tips forward and accelerates, providing more lateral control and allowing the quadrotor to regain control. It is clear that this instability is significantly reduced when using the proposed thrust control.

VI. CONCLUSION

In this paper, we have presented an implicit scheme based on aerodynamic power for computing thrust that can address changes in aerodynamic conditions around individual rotors of fixed-pitch electrically powered multirotor aerial vehicles. A thrust controller was proposed which has similar transient properties to the current RPM-based static model and controller.

Procedures for laboratory calibration of the proposed algorithm are provided based on force–torque measurements. Through static and dynamic flight tests, the power-based thrust modeling scheme along with the controller has been shown to be superior to the RPM-based controller in maintaining a desired thrust setpoint and a desired flight path in the presence of updrafts/downdrafts using the same high-level trajectory/position controller.

APPENDIX

In this section, we prove stability and derive the stability bounds for the hierarchical controller proposed in Fig. 6 of Section III. Recall that in the motor model, M_1 is a combination of (22a) and (22c) and model the nonlinear relationship between v_a and i_a . M_2 is the nonlinear model that relates i_a and the aerodynamic mechanical power P_{am} and M_3 represents the nonlinear model that maps P_{am} to T as outlined in Section II-E. If the linearization about the static hover condition $\bar{M}_1(s)$, $\bar{M}_2(s)$, $\bar{M}_3(s)$ of the motor models M_1 , M_2 , and M_3 expressed as transfer functions, then recall the electrical and mechanical dynamics for a motor–rotor system outlined in (22) (see also [7])

$$v_a = K_e \varpi + i_a R_a + L_a \frac{di_a}{dt}, \quad (31a)$$

$$\tau = (K_{q0} - K_{q1} i_a) i_a, \quad (31b)$$

$$\mathbb{I}_r \dot{\varpi} = \tau - \tau_D \quad (31c)$$

where \mathbb{I}_r is the moment of inertia of the rotor, the aerodynamic torque $\tau_D = C_Q \varpi^2$, where C_Q is the torque coefficient. Around a hover condition, one can approximate $C_Q \varpi^2$ by $\tau_D = \delta \varpi$ with any offset to be dealt with by the feedforward $f_2(T_d)$. Furthermore, we will write $K_q = (K_{q0} - 2K_{q1} i_a^*)$ for the linearization of the effective torque constant at the current i_a^* drawn at hover condition. Combining (31b) and (31c), we get the transfer function of the linear rotor dynamics as $\mathbb{I}_r s \varpi = K_q i_a - \delta \varpi$. From which

$$\varpi = \frac{K_q}{\mathbb{I}_r s + \delta} i_a.$$

To derive the motor model $\bar{M}_1 = \frac{v_a}{i_a}$ shown in Fig. 6, consider the following algebraic process:

$$\begin{aligned} v_a &= K_e \varpi + R_a i_a + L_a \frac{di_a}{dt}, \\ &= K_e \varpi + R_a i_a + L_a s i_a, \\ &= i_a \left(\frac{K_e K_q}{\mathbb{I}_r s + \delta} + R_a + L_a s \right), \\ &= \frac{i_a}{\mathbb{I}_r s + \delta} (K_e K_q + (R_a + L_a s)(\mathbb{I}_r s + \delta)). \end{aligned}$$

Hence

$$\bar{M}_1 = \frac{v_a}{i_a} = \frac{(\mathbb{I}_r s + \delta)(R_a + L_a s) + K_e K_q}{\mathbb{I}_r s + \delta}.$$

To obtain \bar{M}_2 , from (25), recall from (19), the aerodynamic mechanical power $P_{am} = c_3 \varpi^3 + \kappa T \lambda_i \varpi R$. From Section II-D, the linearization of κ is such that $\kappa = \text{const} \frac{1}{C_T} = a \frac{\varpi^2}{T}$, where

a is a constant. Hence

$$P_{am} = c_3 \varpi^3 + a \lambda_i R \varpi^3 = C_{P_{am}} \varpi^3$$

where $C_{P_{am}} = c_3 + a \lambda_i R$. In a similar manner to the ϖ^2 term in τ_D , the cubic term of P_{am} can be linearized around the hover condition, i.e., $\varpi^3 = \varpi_h + \varpi$ and ϖ_h is handled by the feedforward term $f_1(T_d)$, i.e.

$$P_{am} = b_p \left(\frac{K_q}{\mathbb{I}_r s + \delta} \right) i_a$$

where b_p is a positive constant. Hence

$$\bar{M}_2 = \frac{i_a}{P_{am}} = \frac{\mathbb{I}_r s + \delta}{b_p K_q}.$$

To obtain \bar{M}_3 , using the models for thrust and power obtained in (18) and (19), C_T is constant given that c_1 , c_2 , and λ_i are constant with $\lambda_z = 0$, i.e., $T = C_T \varpi^2$. Hence

$$\bar{M}_3 = \frac{P_{am}}{T} = \gamma \varpi = \frac{\gamma K_q}{\mathbb{I}_r s + \delta} i_a$$

where γ is some positive constant.

The next stage in the design is choosing the controller gains and deriving suitable stability bounds. Starting with the inner-loop current control

$$\begin{aligned} H_1(s) &= \frac{i_a}{i_a^d} = \frac{K_p^1 \bar{M}_1}{1 - \bar{M}_1 K_p^1}, \\ &= \frac{K_p^1 [K_e K_q + (R_a + L_a s)(\mathbb{I}_r s + \delta)]}{\mathbb{I}_r s + \delta - K_p^1 [K_e K_q + (R_a + L_a s)(\mathbb{I}_r s + \delta)]}. \end{aligned}$$

The original system \bar{M}_1 has two zeros and a pole which translates into two poles in $H_1(s)$. $H_1(s)$ has a very fast pole as a result of the motor inductance and a slow pole as a result of rotor moment of inertia. Given that the motor control loop runs at 1 kHz, the fast electrical dynamics is within one sample and therefore is beyond the limit of control of the controller. Hence, one can neglect the fast electrical dynamics by setting $L_a = 0$. With this

$$H_1(s) = \frac{K_p^1 [K_e K_q + R_a (\mathbb{I}_r s + \delta)]}{\mathbb{I}_r s + \delta - K_p^1 [K_e K_q + R_a (\mathbb{I}_r s + \delta)]}.$$

Therefore, the characteristic equation of the inner-loop current control is

$$(\mathbb{I}_r - K_p^1 R_a \mathbb{I}_r) s + \delta - K_p^1 (K_e K_q + R_a \delta) = 0$$

from which

$$s = -\frac{\delta - K_p^1 (K_e K_q + R_a \delta)}{\mathbb{I}_r (1 - K_p^1 R_a)}.$$

Hence, for the stability of the closed-loop pole

$$\delta - K_p^1 (K_e K_q + R_a \delta) \geq 0 \text{ and } 1 - K_p^1 R_a > 0$$

giving

$$K_p^1 \leq \frac{\delta}{K_e K_q + R_a \delta} \text{ and } K_p^1 < \frac{1}{R_a}. \quad (32)$$

Since K_e and K_q are positive constants, the second constraint is always satisfied if the first holds. For the motor–rotor system

used, $K_p^{-1} = 0.01$ was found to give the fastest decay time for current or rise time for ϖ .

From the model for \bar{M}_2 and \bar{M}_3

$$\bar{M}_2 \bar{M}_3 = \frac{\gamma}{b_p}.$$

For the outer-loop controller, let this be C , then

$$C = \frac{K_p^2 s + K_i^2}{s} = K \frac{s + z}{s}$$

where the zero gives $z = \frac{K_p^2}{K_i^2}$ and the controller gain $K = K_p^2$. Thus, the closed-loop transfer function for the thrust controller outer loop is

$$H_2(s) = \frac{T}{T_d} = \frac{CH_1 \bar{M}_2 \bar{M}_3}{1 + CH_1 \bar{M}_2 \bar{M}_3}.$$

Thus, the characteristic equation $1 + CH_1 \bar{M}_1 \bar{M}_2 = 0$ for this is

$$\begin{aligned} & (\mathbb{I}_r + K_p^{-1} R_a \mathbb{I}_r + \gamma K K_p^{-1} R_a \mathbb{I}_r) s^2 + (\delta + K_p^{-1} (K_e K_q + R_a \delta) \\ & + \gamma K K_p^{-1} (K_e K_q + R_a \delta + z R_a \mathbb{I}_r)) s \\ & + \gamma K K_p^{-1} (z K_e K_q + z R_a \delta) = 0. \end{aligned} \quad (33)$$

The design for K and z are based on the transient requirements, in this case, a rise time of 20 ms and a settling time of 50 ms as shown in Fig. 10.

Although the stability analysis is developed for a linearized version of the system around hover conditions, the underlying passivity of the aerodynamics and simplicity of the control architecture provides confidence that the resulting controller is highly robust. The expectation was confirmed in practice and the proposed motor-rotor control has proven highly robust and insensitive to parameter error over a very wide range of operating conditions.

ACKNOWLEDGMENT

The authors would like to thank Mr. A. Martin for his contribution to the experimental platform and X. Hou for his insights on tuning the trajectory controller gains.

REFERENCES

- [1] D. Abeywardena, S. Kodagoda, G. Dissanayake, and R. Munasinghe, "Improved state estimation in quadrotor mavs: A novel drift-free velocity estimator," *IEEE Robot. Autom. Mag.*, vol. 20, no. 4, pp. 32–39, Dec. 2013.
- [2] G. Allibert, D. Abeywardena, M. Bangura, and R. Mahony, "Estimating body-fixed frame velocity and attitude from inertial measurements for a quadrotor vehicle," *Proc. IEEE Multiconf. Syst. Control*, 2014, pp. 978–983.
- [3] B. Arain and F. Kendoul, "Real-time wind speed estimation and compensation for improved flight," *IEEE Trans. Aerosp. Electron. Syst.*, vol. 50, no. 2, pp. 1599–1606, Apr. 2014.
- [4] K. J. Åström and T. Hagglund, *Automatic Tuning of PID Controllers*. Pittsburgh, PA, USA: Instrum. Syst. Autom. Soc., 1988.
- [5] Autoquad Team, "The AutoQuad ESC32—Advanced electronic speed controller," 2016. [Online]. Available: <http://autoquad.org/esc32/>, Accessed Nov. 7, 2016.
- [6] R. Bachmayer, L. L. Whitcomb, and M. A. Grosenbaugh, "An accurate four-quadrant nonlinear dynamical model for marine thrusters: Theory and experimental validation," *IEEE J. Ocean. Eng.*, vol. 25, no. 1, pp. 146–159, Jan. 2000.
- [7] M. Bangura, H. Lim, H. J. Kim, and R. Mahony, "Aerodynamic power control for multirotor aerial vehicles," in *Proc. IEEE Int. Conf. Robot. Autom.*, 2014, pp. 529–536.
- [8] M. Bangura, H. Lim, H. J. Kim, and R. Mahony, "An open-source implementation of a unit quaternion based attitude and trajectory tracking for quadrotors," in *Proc. Australas. Conf. Robot. Autom.*, 2014, pp. 1–10.
- [9] M. Bangura and R. Mahony, "Nonlinear dynamic modeling for high performance control of a quadrotor," in *Proc. Australas. Conf. Robot. Autom.*, 2012, pp. 1–10.
- [10] M. Bangura and R. Mahony, "Real-time model predictive control for quadrotors," in *Proc. 19th IFAC World Congr.*, 2014, pp. 11773–11780.
- [11] M. Bangura, M. Melega, R. R. Naldi, and R. Mahony, "Aerodynamics of rotor blades for quadrotors," *arXiv:1601.00733*, pp. 11773–11780, 2016.
- [12] A. R. S. Bramwell and D. Balmford, and G. Done, *Bramwell's Helicopter Dynamics*. Amsterdam, The Netherlands: Elsevier, 2001.
- [13] H. Glauert, *The Elements of Aerofoil and Airscrew Theory*. Cambridge, U.K.: Cambridge Univ. Press, 1983.
- [14] A. J. Healey, S. M. Rock, S. Cody, D. Miles, and J. P. Brown, "Toward an improved understanding of thruster dynamics for underwater vehicles," *IEEE J. Ocean. Eng.*, vol. 20, no. 4, pp. 354–361, Oct. 1995.
- [15] M-D. Hua, T. Hamel, P. Morin, and C. Samson, "Introduction to feedback control of underactuated vtol vehicles: A review of basic control design ideas and principles," *IEEE Control Syst.*, vol. 33, no. 1, pp. 61–75, Feb. 2013.
- [16] J. Y. Hwang, M. K. Jung, and O. J. Kwon, "Numerical study of aerodynamic performance of a multirotor unmanned-aerial-vehicle configuration," *J. Aircr.*, vol. 52, no. 3, pp. 839–846, 2014.
- [17] V. Kumar and N. Michael, "Opportunities and challenges with autonomous micro aerial vehicles," *Int. J. Robot. Res.*, vol. 31, no. 11, pp. 1279–1291, 2012.
- [18] J. G. Leishman, *Principles of Helicopter Aerodynamics* (Cambridge Aerospace Series). Cambridge, U.K.: Cambridge Univ. Press, 2002.
- [19] J. Luo, L. Zhu, and G. Yan, "Novel quadrotor forward-flight model based on wake interference," *AIAA J.*, vol. 53, no. 12, pp. 3522–3533, 2015.
- [20] S. Lupashin, A. Schollig, M. Sherback, and R. D'Andrea, "A simple learning strategy for high-speed quadcopter multi-flips," in *Proc. IEEE Int. Conf. Robot. Autom.*, 2010, pp. 1642–1648.
- [21] R. Mahony, V. Kumar, and P. Corke, "Multirotor aerial vehicles: Modeling, estimation, and control of quadrotor," *Robot. Autom. Mag.*, vol. 19, no. 3, pp. 20–32, 2012.
- [22] P. Martin and E. Salaün, "The true role of accelerometer feedback in quadrotor control," in *Proc. IEEE Int. Conf. Robot. Autom.*, May 2010, pp. 1623–1629.
- [23] D. Mellinger, N. Michael, and V. Kumar, "Trajectory generation and control for precise aggressive maneuvers with quadrotors," *Int. J. Robot. Res.*, vol. 31, pp. 664–674, 2012.
- [24] S. Omari, M-D. Hua, G. Ducard, and T. Hamel, "Nonlinear control of vtol uavs incorporating flapping dynamics," in *Proc. IEEE/RSJ Int. Conf. Intell. Robots Syst.*, 2013, pp. 2419–2425.
- [25] L. Pivano, T. A. Johansen, and O. N. Smogeli, "A four-quadrant thrust estimation scheme for marine propellers: Theory and experiments," *IEEE Trans. Control Syst. Technol.*, vol. 17, no. 1, pp. 215–226, Jan. 2009.
- [26] P. Pounds, *Design, Construction and Control of a Large Quadrotor Micro Air Vehicle*. Ph.D. thesis, Faculty of Engineering, Australian National Univ., Acton, ACT, Australia, Sep. 2007.
- [27] P. Pounds, R. Mahony, and P. Corke, "Design of a static thruster for micro air vehicle rotorcraft," *ASCE J. Aerosp. Eng.*, vol. 22, no. 1, pp. 85–94, Jan. 2009.
- [28] S. Shen, N. Michael, and V. Kumar, "Obtaining liftoff indoors: Autonomous navigation in confined indoor environments," *IEEE Robot. Autom. Mag.*, vol. 20, no. 4, pp. 40–48, Dec. 2013.
- [29] JR3 Team, "Jr3: Multi-axis load cell technologies," 2016. [Online]. Available: <http://www.jr3.com/>, Accessed Nov. 7, 2016.
- [30] S. L. Waslander and C. Wang, "Wind disturbance estimation and rejection for quadrotor position control," in *Proc. AIAA Infotech Aerosp. Conf. AIAA Unmanned Unlimited Conf.*, 2009, pp. 1935–1948.
- [31] D. W. Yeo, N. Sydney, D. A. Paley, and D. Sofge, "Onboard flow sensing for downwash detection and avoidance with a small quadrotor helicopter," in *Proc. AIAA Guid. Navigat., Control Conf.*, 2015, pp. 1–1.



Moses Bangura received the Bachelor of Engineering degree with first class honors in aeronautical (space) engineering from The University of Sydney, Sydney, Australia in 2010 and the Ph.D degree in aerial robotics at the Australian National University, Canberra, Australia.

Between his undergraduate and doctoral studies, he was with the Defence Science and Technology Organisation as a Modelling and Simulation Analyst. He is currently a Postdoctoral Research Fellow with the Robotics Institute, Carnegie Mellon University,

Pittsburgh, PA, USA. His research interests include state estimation, nonlinear and robust control applied to unmanned aerial vehicles.



Robert Mahony received the Ph.D. degree in systems engineering from the Australian National University, Canberra, Australia, in 1995, after originally training in geophysics and working in marine seismology.

He is a Professor in the Research School of Engineering, Australian National University. His research interests include nonlinear systems theory, and optimization with applications in robotics and computer vision.